11

Magnetic anomalies of terrain-delimited magnetisations in northern New South Wales as a training set for Martian magnetic field mapping

C.A. Foss and J.R. Austin

ABSTRACT

Total magnetic intensity (TMI) variations measured by an aeromagnetic survey over the Miocene age Lamington Volcanics in northern New South Wales are well explained by inversion of homogeneously magnetised digital terrain models. At different locations these models variously have normal magnetisation and magnetisation dominated by reverse remanence. In consequence of closely matching measured TMI variation the orthogonal magnetic field components forward computed from these terrain models also closely match the equivalent components derived from frequency-domain transform (FFT) of measured TMI. We show that terrain magnetisations can be reasonably recovered from inversion of three-component magnetic field data along single traverses using the constraint of an independently known spatial model. For measurements of limited spatial distribution such as along isolated flight paths, along rover tracks or at dispersed landing sites, multi-component data provide additional information to single-component data. Direct measurement of magnetic vector components in the Earth's strong background field incurs prohibitive errors arising from even slight sensor misorientation. However, these penalties are much smaller where background fields are weak. Furthermore, in weak background fields the direction of the total field varies considerably across and around anomalies, and for magnetic field mapping this makes TMI less suitable than vector components of consistent direction. We assign the normal and reverse magnetisations estimated from the Tenterfield modelling study to an isolated topographic feature of width 23 km and height 800 m to the north of the Argyre Basin region of Mars and are able to reasonably recover those magnetisation directions from multi-component inversion of emulated data on short flight-paths over the feature and sparse station measurements on rover tracks around it. The success of such survey methods will depend on the validity of a homogeneous magnetisation terrain model and the dominance of the field from that magnetisation across the range of measurement locations.

11.1 INTRODUCTION

Many igneous rocks form positive topographic features where they have been emplaced by eruptions over the land surface or where surrounding less resistive materials have been eroded away. We show that in northern New South Wales the magnetic field variation measured by an aeromagnetic survey over the Lamington volcanics (Duggan and Mason 1978) can be well explained by digital terrain models assigned a homogeneous magnetisation. Over parts of the region there is strong positive correlation between the magnetic field and terrain elevation. For these areas the best estimated magnetisation direction is close to that of the present geomagnetic field. Over other parts of the region there is strong negative correlation between the magnetic field and terrain elevation revealing that magnetisation is dominated by reverse remnant components almost anti-parallel to the present field. We show that in both cases there is close agreement between magnetic field components forward computed from the magnetic terrain models and those transformed from the measured total magnetic intensity (TMI) data. For these sufficiently sampled fields there would be limited advantage in having multi-component data. However, multiple components do provide advantage if the magnetic field is sparsely sampled. On Earth, direct measurement of vector components of the magnetic field is penalised by large errors from misalignment of sensors, primarily arising from a background field that is much stronger than the anomalies of interest (almost 54,000 nT in this study area in north-west New South Wales). The Martian magnetic field dynamo has switched off (e.g. Schubert *et al.* 2000; Mittelholz *et al.* 2020) leaving anomalies largely due to remnant magnetisation in a weak background field. Lack of a strong background field causes the TMI vector to change direction within and around local anomalies. TMI measurements owe their value more from being an (approximately) uni-directional vector measurement than being a (pseudo-) scalar measure of the strength of the field. Where unlocked from the consistent direction of a dominant background field, TMI measurements lose some of their appeal for magnetic field mapping. In low background fields such as those found on Mars this provides advantages for multiple vector component or multiple vector gradient (tensor element) measurements. We selected a Martian topographic feature, assigned it the same magnetisations estimated in the Tenterfield study in northern New South Wales, and forwarded computed its vector component anomalies on the assumption that it is surrounded by material of much weaker magnetisation. If Mars has such isolated and terrain-bound magnetisations then it may be possible to derive large-volume estimates of their mean magnetisation from a sparser set of magnetic field measurements than is required for buried sources of unknown position, orientation and extent. Optimisation of magnetic field measurement is of critical advantage in an environment where it is not feasible to measure the field as extensively as we do on Earth.

11.2 TERRAIN-BOUND MAGNETISATIONS AT TENTERFIELD, NEW SOUTH WALES

Figure 11.1 shows the location of part of the 100,000 line kilometre Grafton-Tenterfield regional aeromagnetic survey (Geoscience Australia GADDS survey P1252) flown for the Geological Survey of New South Wales in 2011 using a Cessna 404 fixed wing aircraft on east–west flightlines at 250 m line spacing and with a nominal ground clearance of 60 m. The actual ground clearance is highly variable because of the rugged terrain. The survey extends to the Queensland border and covers an area known as 'the Scenic Rim'. TMI and DEM mapping from the survey data are imaged in Fig. 11.2. The magnetic field strength varies by over 1,600 nT and the variation in elevation is over 800 m. Shown in Fig. 11.2 are the outlines of two detailed study areas. In the north-east area there is a clear negative correlation between ground elevation and TMI, and in the south-west area there is a strong positive correlation between elevation and TMI. The moderately steep geomagnetic inclination of −58° causes a predominantly positive TMI anomaly over a body with magnetisation in the same direction as the field (a 'normal' magnetisation). For terrain-bound magnetisations in contrast against air, any negative correlation between terrain and magnetic field intensity is due to rocks with predominant reverse remanent magnetisation. In the south-west area where there is positive correlation between TMI and terrain either the remanent magnetisation is normal or, if reverse, it is weaker than the induced magnetisation. Our preferred interpretation is that remanent magnetisation and magnetic susceptibilities are similar in both areas, with difference in polarity of the remanent

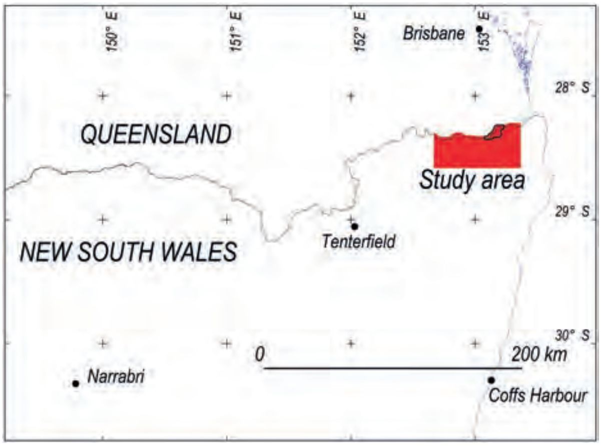

Fig. 11.1. Location of the Tenterfield study area.

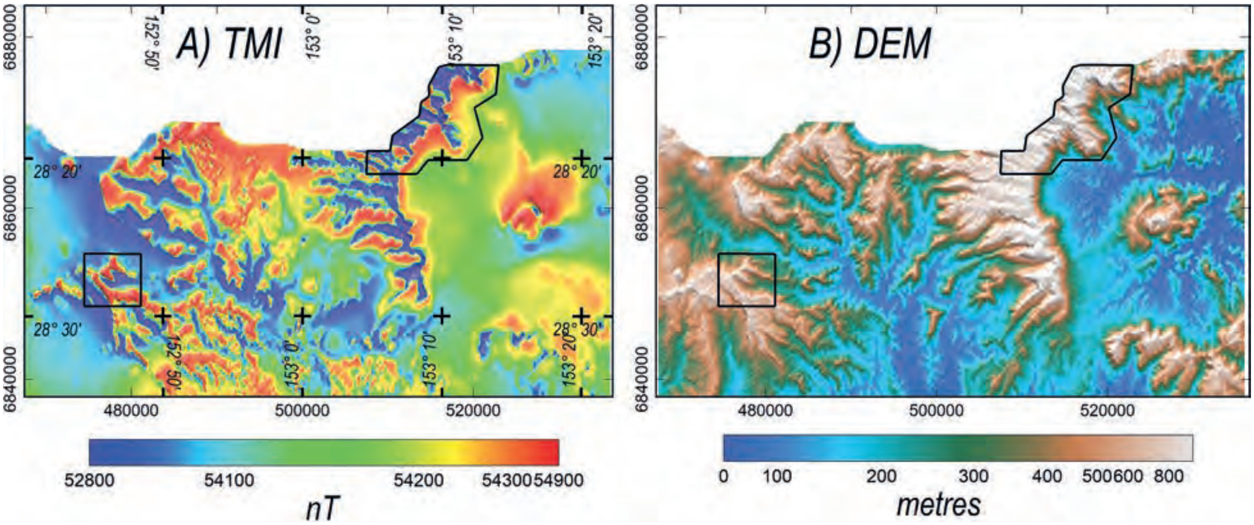

Fig. 11.2. A) TMI and B) DEM images of the Tenterfield area of north-east New South Wales with the two study areas highlighted.

magnetisation due to slight age differences that span a reversal of the Earth's magnetic field.

For the two study areas in Fig. 11.2 we built separate magnetisation models using the terrain surface as the upper surface of magnetisation and a horizontal surface approximately coincident with the base of the Lamington Volcanics as mapped by Brown *et al.* (2007) as the base of magnetisation. The terrain image for the north-east area is shown in Fig. 11.3A and the faceted, closed volume model generated from that surface and the nominated horizontal base level is shown in Fig. 11.3B. For each area we emulated the background magnetic field (the field that would be expected if the terrain magnetisation was absent) using a second-order polynomial of low curvature. Following the recognised correlations of terrain and TMI noted above, we assigned an initial magnetisation parallel to the local geomagnetic field to the model in the south-west area and a magnetisation anti-parallel to the local geomagnetic field to the model in the north-east area. We then trialled several estimates of magnetisation strength to quickly produce modelled field variations of similar amplitude to the measured TMI variation. This provided starting matches between the measured data and model fields that were close enough to ensure rapid and stable convergence of inversion. The inversions were also naturally stable because the only free parameters were their bulk magnetisations. In the initial inversions of each area only three parameters were free to very: the strength, declination and inclination of magnetisation. Subsequently, the level of the background field and its north–south and east–west planar gradients (another three parameters) were also set free to search for any reduction of data misfit by adjustment of our initial estimate of the background field. The close fit of measured and post-inversion model computed fields in the north-east area is shown in Fig. 11.4. This is strong testament to the general validity of representing this terrain with a magnetisation that is homogeneous in strength and direction. Non-uniqueness generally imposes considerable constraints on such claims of the validity of inversion models, but because the location and extent of magnetisation are locked in place by the terrain surface there is little scope to propose any broad-scale departure from the model (that undoubtedly deviates considerably from the true ground magnetisation at any discrete location). For the reverse-magnetisation north-east area the optimum magnetisation estimate is 3.8 A/m, declination 188° and inclination +57°. This direction is 178° from the local geomagnetic field direction (only 2° from being anti-parallel to it).

Figure 11.5A shows the terrain image and Fig. 11.5B the corresponding faceted terrain model for the south-west area. The match between measured and model computed TMI achieved by inversion of magnetisation for this model shown in Fig. 11.6 is similar to that for the north-east area shown in Fig. 11.4, revealing no difference in performance of inversion for the different magnetisation directions. The optimum magnetisation estimate for the south-west area model is 4.2 A/m,

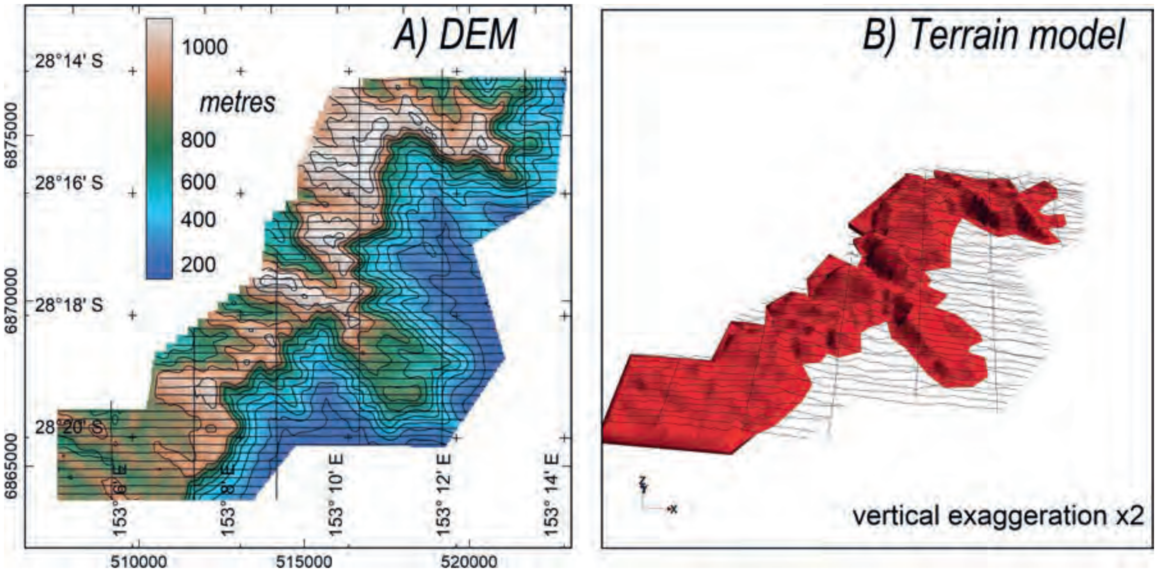

Fig. 11.3. A) terrain elevation and B) the corresponding terrain model and survey flightlines for the north-east area.

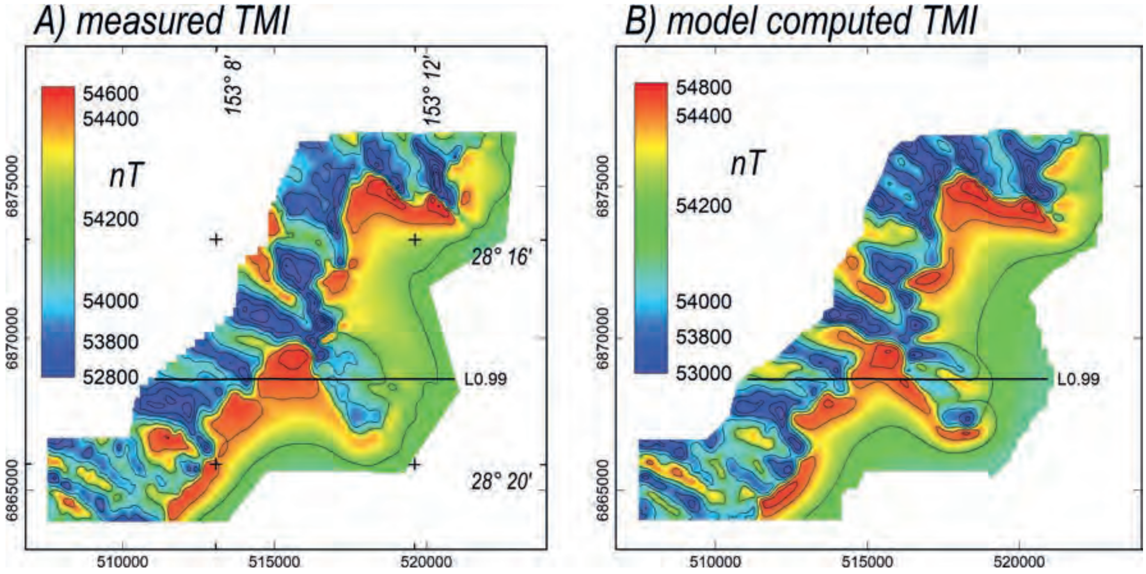

Fig. 11.4. A) measured TMI and B) model forward computed TMI for the (reverse magnetisation) north-east area.

declination 18° and inclination −54°. This direction is 6° from the local geomagnetic field direction and 6° from being anti-parallel to the magnetisation direction in the north-east area. Note that the resultant magnetisation directions for the two areas are not expected to be exactly anti-parallel unless the remanence directions are exactly anti-parallel to each other and also parallel and anti-parallel to the induced magnetisation. Using simple addition and subtraction of the two model magnetisations the best estimates of common magnetic properties for the two areas are: susceptibility 0.014 SI, remanent magnetisation intensity 4.0 A/m and Koenigsberger ratio 7. However, those estimates are dependant on assumptions of conformity of magnetisation between the two areas and across large model volumes. The model estimates are likely to have little significance to magnetisations that would be measured on single rock samples.

Figure 11.7 shows example flightline sections over the post-inversion models from each of the two areas (for locations see Figs 11.3 to 11.6). Note that the data misfits shown in Fig. 11.7 are not optimised to the data only along those specific lines but to all the lines in each

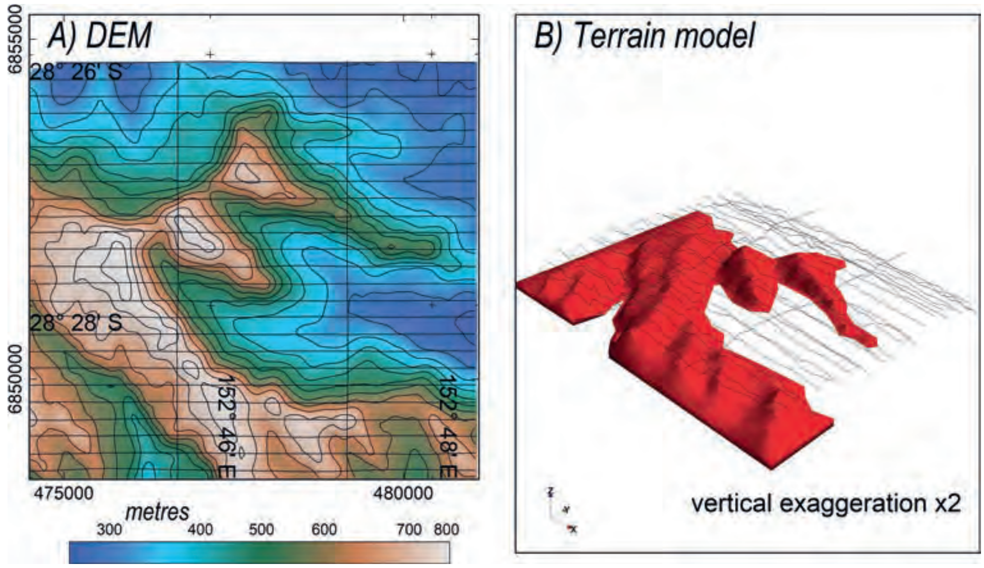

Fig. 11.5. A) terrain elevation and B) the corresponding terrain model and survey flightlines for the south-west area.

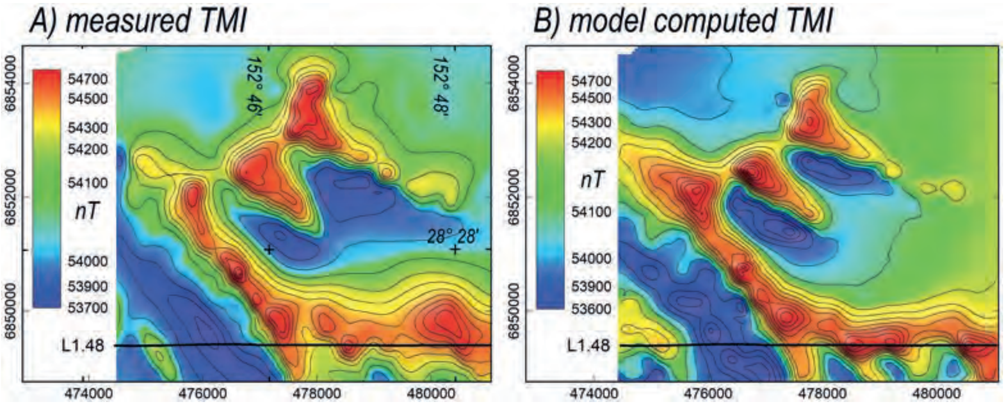

Fig. 11.6. A) measured TMI and B) model forward computed TMI for the (reverse magnetisation) north-east area.

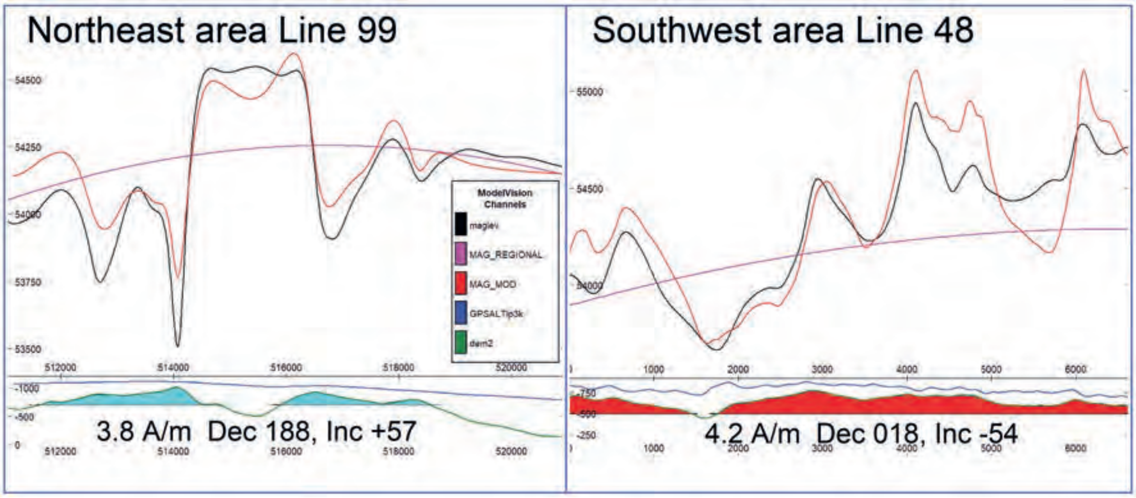

Fig. 11.7. Individual inversion model sections A) from the (reverse magnetisation) north-east area model and B) from the (normal magnetisation) south-west area model.

area. Matching the data on only those single lines would reduce the displayed data misfits on those lines, but the significance of the changes to the models to achieve that would be uncertain. Selection of large model areas with multiple flightlines of considerable length stabilises estimation of the mean magnetisation but it also increases concerns of that magnetisation poorly representing subareas. Further reduction of the misfit between the measured and model computed fields could be achieved by adding local detail to the models but any such changes would require validation.

11.3 TENTERFIELD SURVEY MULTIPLE COMPONENT ANALYSIS AND INVERSION

Magnetic field surveys measure TMI not for interpretational advantage but because of the convenience of low sensitivity to sensor orientation. In almost all surveys, measured TMI values are indistinguishable from the value of the vector in the local geomagnetic field direction (exceptions are for surveys of particularly high-amplitude variations in which there are local rotations of the TMI direction). Assuming that TMI is consistently directed and is therefore a potential field (Blakely 1995) it can be converted to a vector in any other direction using an FFT phase transform (as noted by Blakely 1995 this transform may be unstable for certain combinations of angles if the input data is noisy). TMI can for instance be converted with three different phase transforms to the set of east, north and vertical field components B_x, B_y, B_z. The conditions are that the field is sampled at close spacing and high resolution across a sufficient distance to faithfully treat the range of wavelengths present. These transforms modify the data but do not add information to them. In practice they introduce distortion because of their dependence on the gridding process and (of particular relevance to the Tenterfield survey) on any irregularity in elevation of the measurement surface. Figure 11.8 shows on the top row the B_x, B_y, B_z components forward computed from the TMI inversion model (these three orthogonal components are computed as an intermediate step in calculation of TMI). The bottom row of Fig. 11.8 shows the equivalent components derived by FFT from TMI. Because the model matches

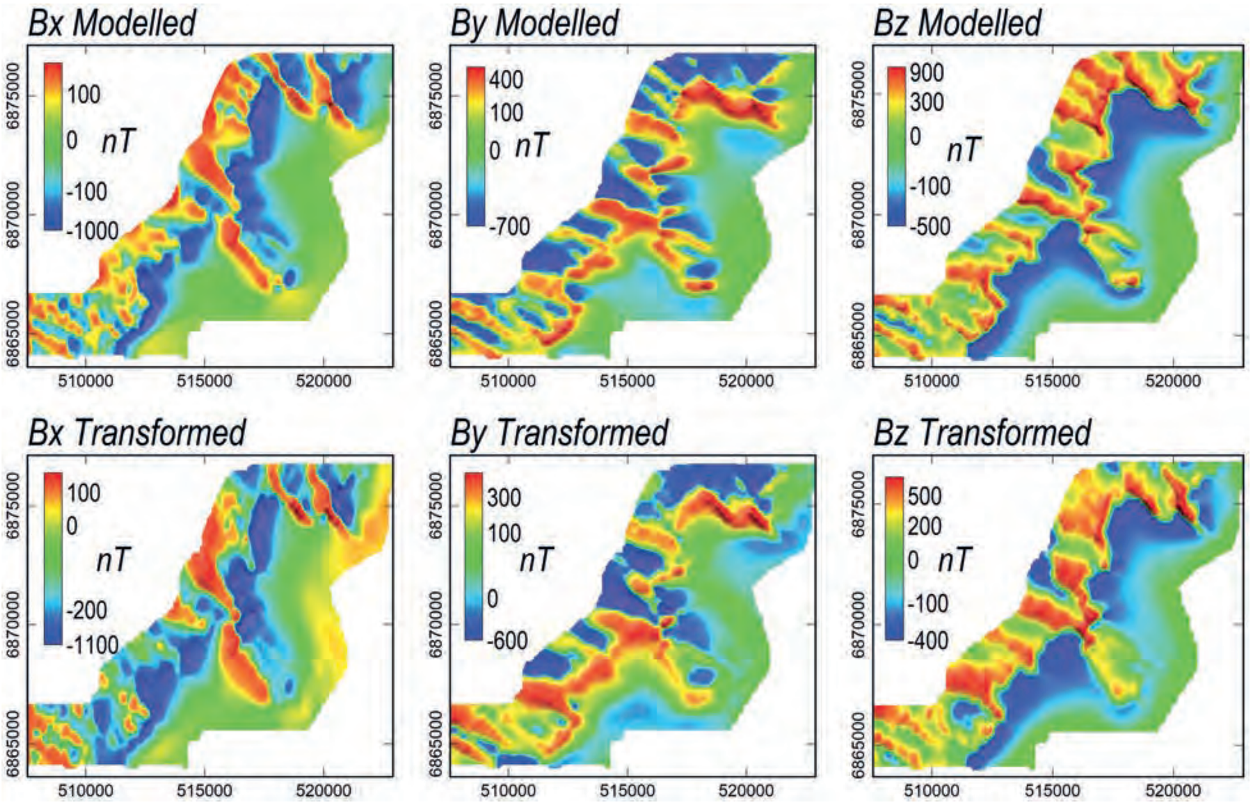

Fig. 11.8. (Left column) Inversion model computed B_x, B_y and B_z components, and (right column) equivalent FFT transformed components for the north-east reversely magnetised area.

the TMI data across a wide area the model components approximately match the same components derived by phase transform of the TMI. Component transforms are independent of magnetisation direction and Fig. 11.9 shows the same predictive success of the FFT components in matching the model components for the reverse magnetisation area.

There is no information gained in transforming the TMI grid data to the different component grids. However, for a restricted distribution of data, such as a single flightline, there is advantage in having multiple magnetic field components and/or gradients. Figure 11.10 shows single flightline magnetisation inversions of the two terrain models. Line 99 is from the south-west model and line 48 is from the north-east model. The top panel in Fig. 11.10 shows measured TMI (solid lines), model-computed TMI from the all-line TMI inversions (dashed lines) and model-computed TMI from the single-line TMI inversions (dotted lines). The dedicated single line inversions fit the data more closely because the data-fit is optimised to only those single lines but the multi-line inversions also fit most features on those lines quite closely. This stability of the inversions is largely due to constraint of the spatial variation of magnetisation from the terrain-model.

The magnetic field component panels (B_x, B_y, B_z) in Fig. 11.10 show (solid lines) the input data from FFT phase transform of the measured TMI grid interpolated onto the lines, (dashed lines) the component forward computed from the all-line TMI inversion, and (dotted lines) the component forward computed from the single flightline component inversions. The inversion magnetisation direction estimates are plotted in Fig. 11.11. The all-line inversions produce the most consistent magnetisation estimates (plotted with triangular symbols in Fig. 11.11). Note that the closed symbols (normal magnetisations) are on the opposite hemisphere to the open symbols (reverse magnetisations). The smaller symbols in Fig. 11.11 are magnetisation directions from the single line, single component (including TMI) inversions. These directions are reasonably clustered with mean departures from the average values of 11° and 13°

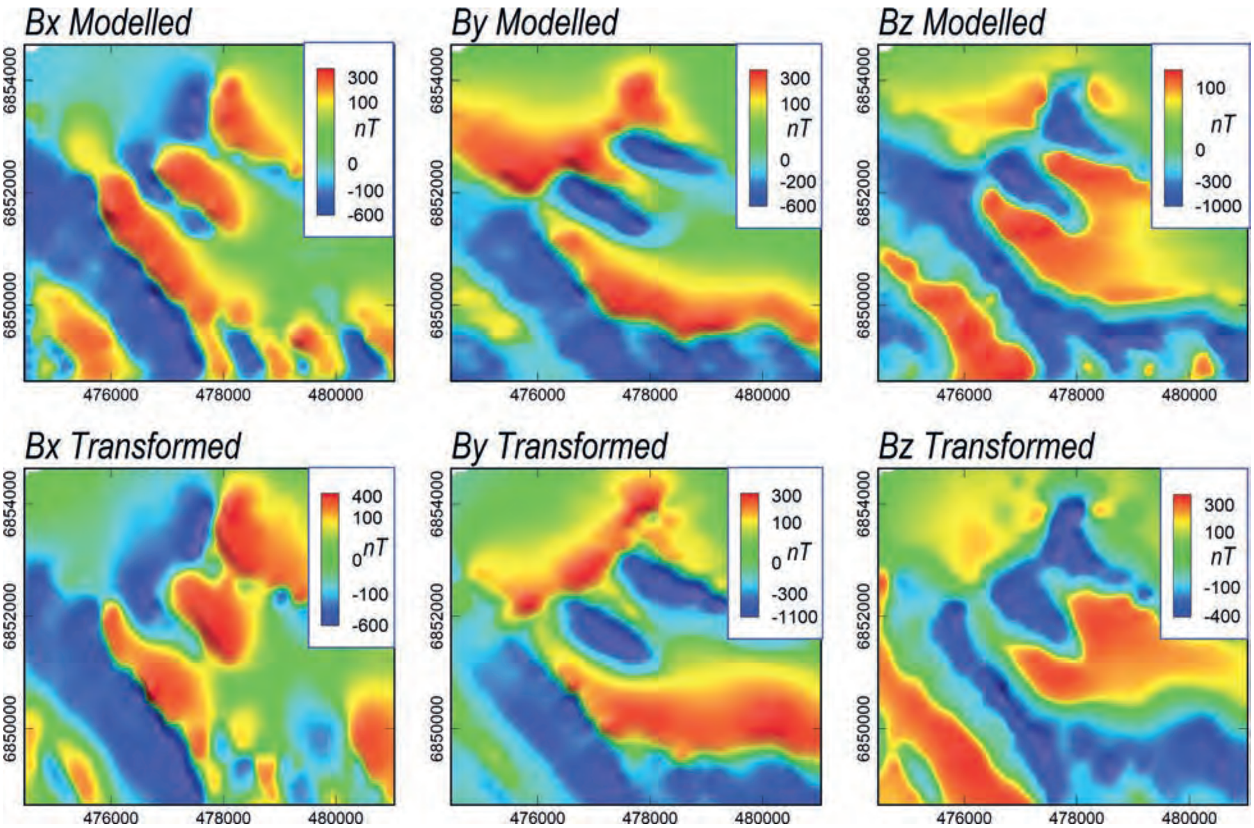

Fig. 11.9. (Left column) Inversion model computed Bx, By and Bz components, and (right column) equivalent FFT components for the south-west normally magnetised area.

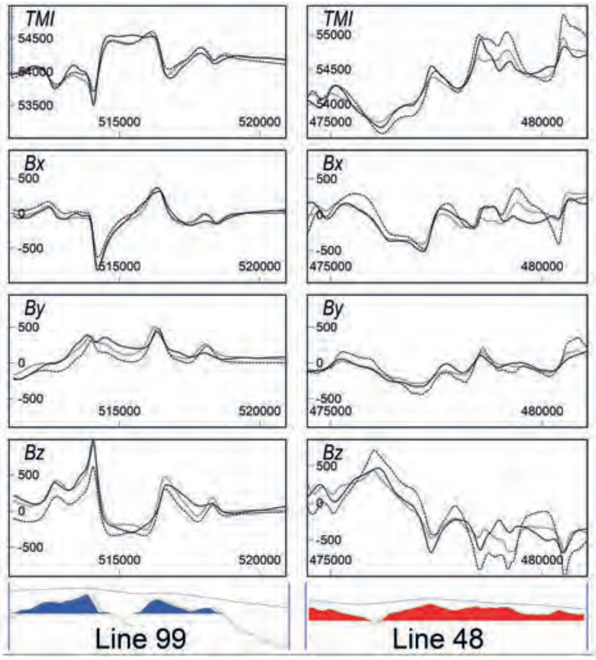

Fig. 11.10. Single flightline inversions of TMI and Bx, By and Bz components. The solid line is the input channel measured TMI and FFT transformed components, the dashed line is the output channel of the complete areas TMI inversions and the dotted lines are the output channels of the different component single flightline inversions.

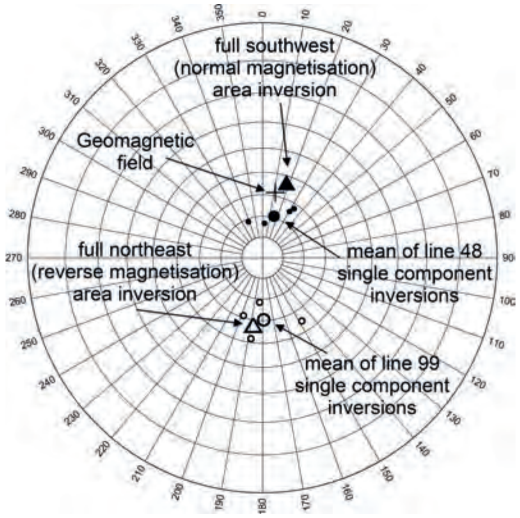

Fig. 11.11. Inversion magnetisation directions (negative inclination 'normal' directions as closed symbols and positive inclination 'reverse' directions as open symbols). Triangles are all-area TMI inversion directions, the larger circles are the means of the invididual component single-line inversions (small symbols).

for the normal and reverse magnetisations respectively, and those means are 6° and 15° from the all-lines inversion directions. These results indicate that using the terrain-model constraint a reasonable magnetisation estimate can be obtained from inversion of an individual magnetic field component on a single flightline. Note that if the constraint of the terrain model was not available (for instance if the top of magnetisation was buried by a non-magnetic cover) this would not be possible. Inversion of two or more components along flightlines improves magnetisation direction estimates not just from averaging of results as shown here, but also through joint inversion in which models simultaneously explain the multiple data channels.

11.4 SYNTHETIC MARTIAN TERRAIN MODEL STUDY

Figure 11.12 shows the location (322.2°E, 23.5°S) of an isolated terrain feature north of the Argyre Basin and 160 km south-east of the centre of Roddy Crater. The terrain data is the Mars MGS MOLA DEM (version 2) derived from measurements by the Mars Orbital Laser Altimeter (Smith *et al.* 2001) flown on the Mars Global Surveyor spacecraft (Albee *et al.* 2001) and processed by Neumann *et al.* (2001) and Neumann *et al.* (2003). The feature has a width of 20–25 km and a maximum height above the surrounding ground of 800 m. We select the feature solely as being of convenient size and compactness for this study (small enough to be considered a surface detail but large enough to be well sampled by the 463 m cell-size DEM). From the recent MAVEN magnetic field data acquired at elevations as low as 130 km above surface, Mittelholz *et al.* (2020) report an absence of strong magnetisation over the Argyre Basin but heterogeneous magnetisations in surrounding regions. Derivation of magnetisation from terrain models is scale independent provided it is meaningful to estimate bulk magnetisation values over the selected area. Mostly, we envisage the methods as suitable for surface exploration of small-scale features. In the absence of a known magnetisation we chose the estimates derived at Tenterfield of strength 4.2 A/m, declination 18°, inclination −54° (magnetisation 'A') and the almost anti-parallel magnetisation ('B') of strength 3.8 A/m, declination 188°, inclination +57°. The terrain grid feature is shown in Fig. 11.13A. Figure 11.13B shows the faceted terrain model derived (using ModelVision software) from the grid and a horizontal base surface that we used to forward compute the magnetic field. Figure 11.13C shows a simple three-dimensional polyhedral body (a ModelVision 'frustum' class body) also used as an approximate representation of the terrain.

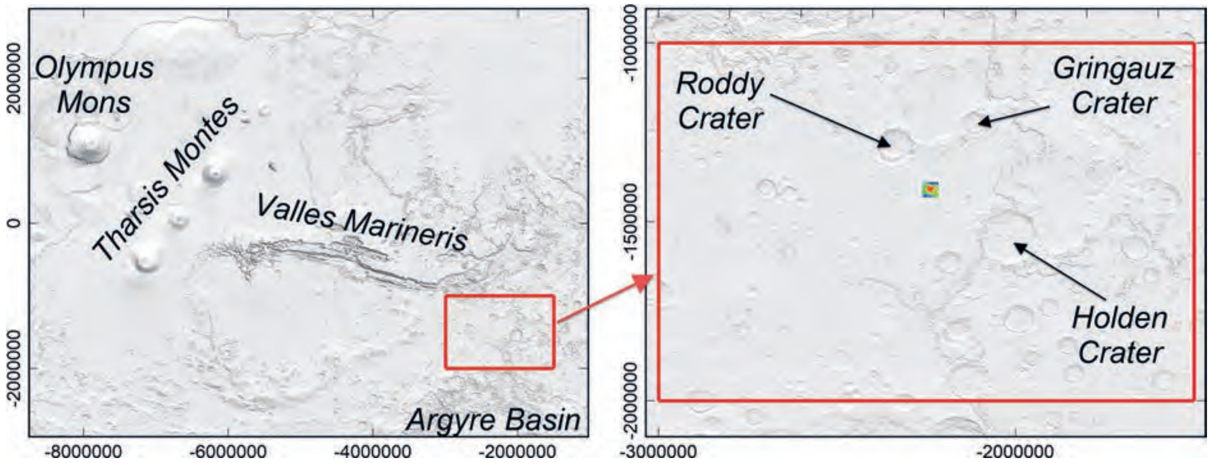

Fig. 11.12. Location of the synthetic terrain magnetic study.

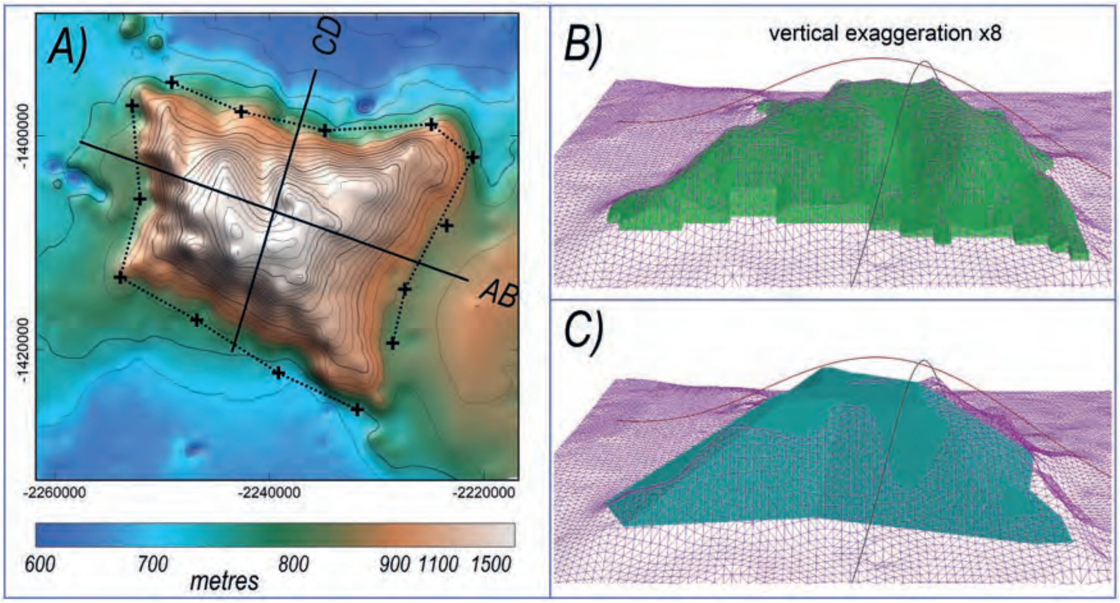

Fig. 11.13. A) terrain image of the isolated topographic feature of study, B) faceted horizon-base model of the terrain feature used for forward field computation, C) polyhedral terrain-approximation model used for inversion.

Figure 11.14 shows magnetic component maps computed just above the ground surface from the detailed terrain model using the two assigned magnetisations. The contour interval is 10 nT and the images have been clipped to exclude the higher amplitude field variations directly above the feature. If there are no overlapping fields and measurements can be made with sufficient resolution, only a sparse distribution of multi-component magnetisations is required to resolve the direction of magnetisation from the mapped fields. Figure 11.14 shows that each magnetic field component switches polarity between fields of the two almost anti-parallel magnetisations (magnetisation A in the top row and magnetisation B in the bottom row). The decrease in B_z on approaching the terrain feature from any direction as shown in the righthand top frame in Fig. 11.14, reveals that the inclination of magnetisation is negative. The greater challenge of characterising magnetisation direction from magnetic field mapping of TMI is illustrated in Fig. 11.15 in which the azimuth of the magnetic field is imaged as it swings around the terrain feature and there is no consistency as with the B_z component in Fig. 11.14 from which to quickly determine the polarity of magnetic inclination. Vector magnetic field measurements require reference orientations. The vertical reference is easily obtained and there are various options for a

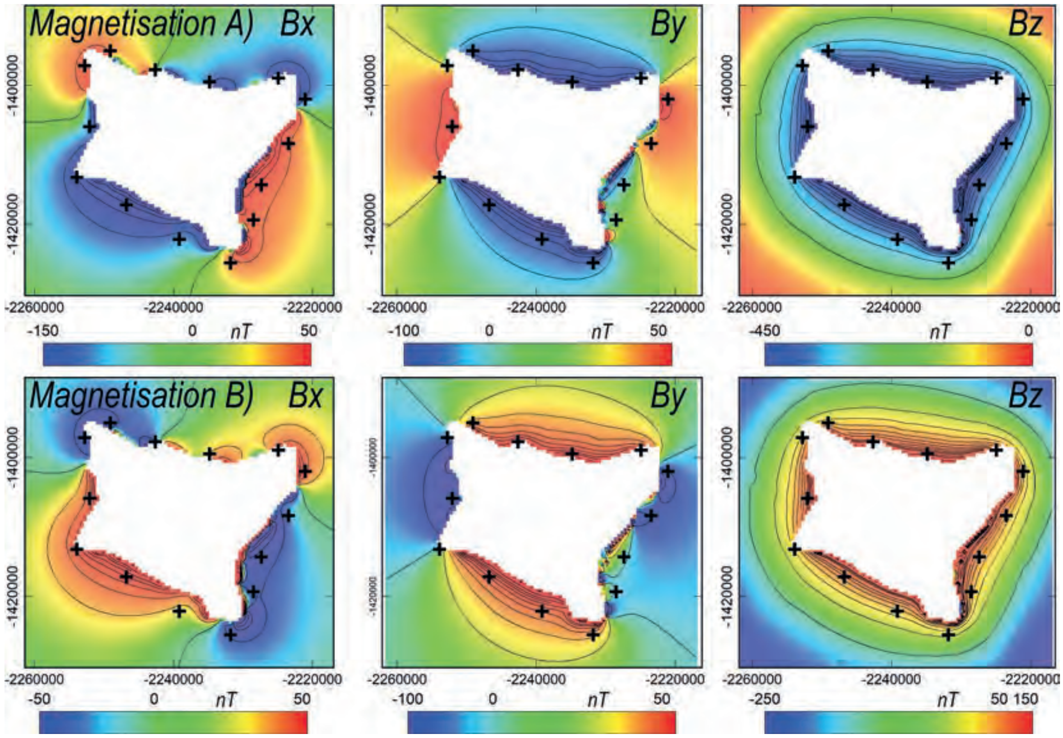

Fig. 11.14. Magnetic field components computed from the terrain model. Upper row for a magnetisation of declination 18°, inclination −54° (magnetisation A) and lower row for a magnetisation of declination 188°, inclination +57° (magnetisation B).

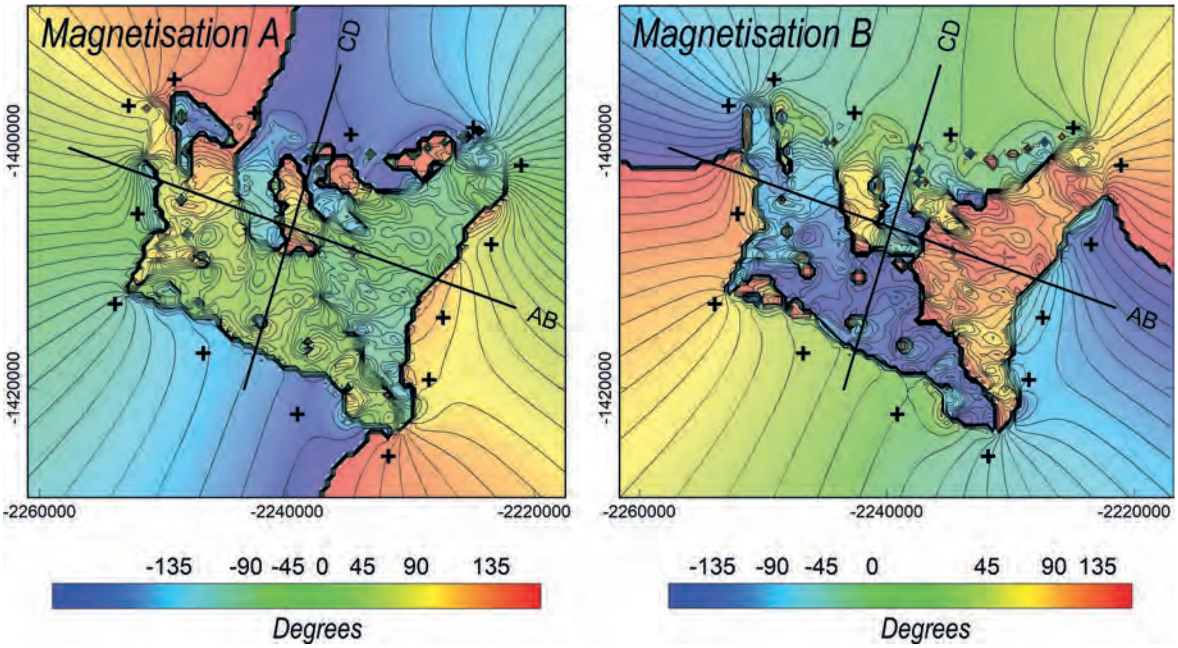

Fig. 11.15. Field declination maps generated by the terrain model fields with (left) magnetisation A and (right) magnetisation B.

horizontal reference, including sun shadows (just as a sun compass is used to orient palaeomagnetic samples).

The horizontal component grid images plotted in Fig. 11.14 all show approximate symmetry about two orthogonal axes. A traverse starting at any point and half-encircling the feature fully samples the component anomaly patterns that express the magnetisation direction. If the anomaly is isolated from other magnetic field variations, four equi-spaced multi-component measurements half-circling the terrain feature are sufficient to recover an estimate of its magnetisation direction. Exact location of the stations is not critical, but stations closer to the feature have stronger signal. We computed magnetic component values 3 m above terrain at six stations on the western track and eight stations on the eastern track (at approximately 8 km intervals) as marked by crosses in Figs 11.13 to 11.15. The traverses start and end near the north-west and south-east corners of the terrain feature. We computed the magnetic component values using the detailed terrain model assigned the magnetisations of ~4 A/m estimated in the Tenterfield study. The average range of the components on each track is 54 nT with a standard deviation of 19 nT. We added noise with a standard deviation of 4 nT to each channel and separately inverted the data along each track with multi-channel (three-component) inversions of the simplified frustum terrain model. Figure 11.16 shows the terrain model computation, model computation with noise and inversion model computation of the three magnetic field components along the two tracks. The four magnetisations recovered from the inversions (for the two tracks and the two magnetisations) are listed in Table 11.1 and plotted in Fig. 11.18. The mean error of the magnetisation estimates is 7°. These results suggest that it should be possible to recover magnetisation estimates on a rover track around an isolated terrain feature if the terrain model of that feature reasonably represents the distribution of a homogeneous magnetisation of at least moderate strength, if there are no other strong magnetisations nearby and if the measurements can be made to a resolution better than 4 nT.

We also emulated three-component magnetic field data collected on two traverses above the feature (as shown in Figs 11.13B and 11.13C) of length 38.5 km and 27.5 km, at ~350 m above the ground and 500 m spacing along the traverses. Magnetisation estimates derived for the homogeneously magnetised terrain feature would benefit only slightly from more closely spaced measurements, but closer measurement spacing would help resolve any local inhomogeneities in magnetisation.

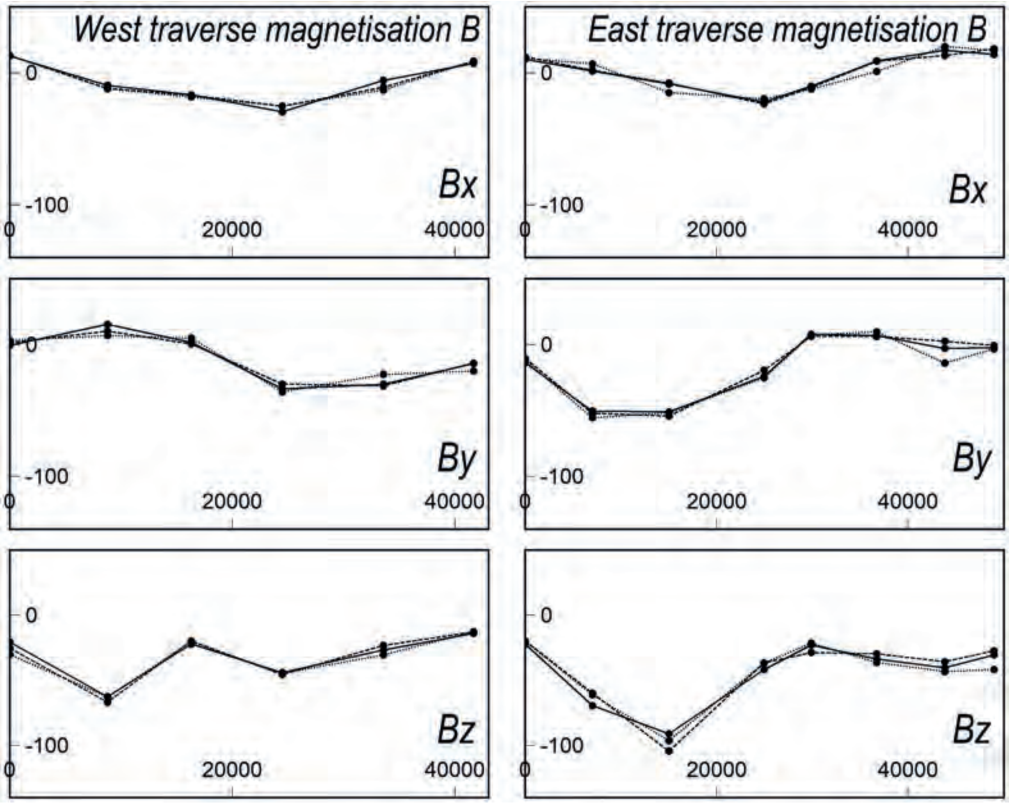

Fig. 11.16. Three-component profiles at stations on west and east tracks with magnetisation B. The three curves of detailed terrain-model compution with and without 4 nT added noise and the simple terrain-model inversion of the noise-added data all form a close envelope.

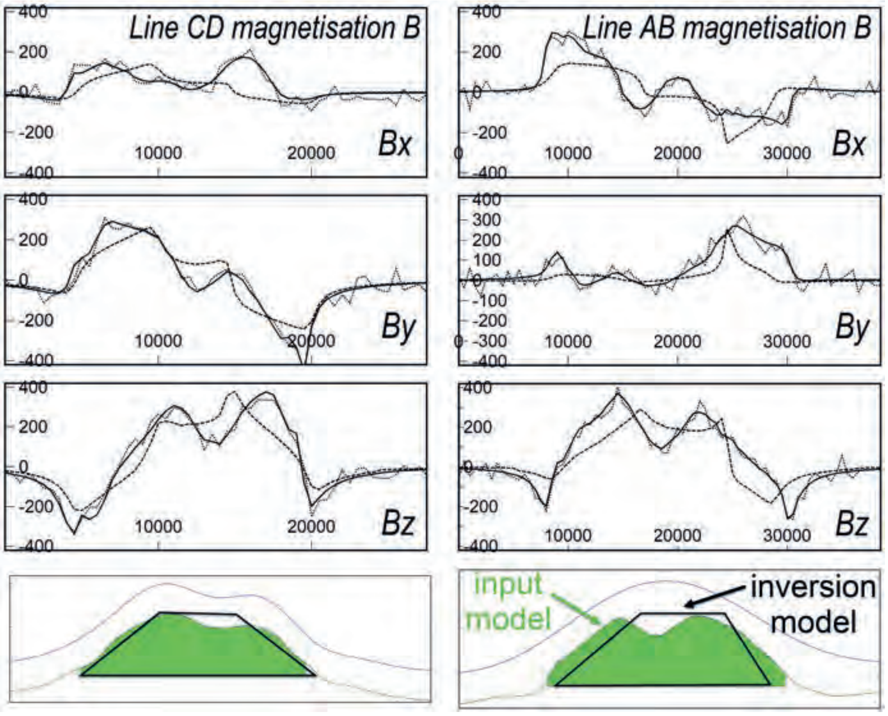

Fig. 11.17 Three component profiles on flightlines AB (right column) and CD (left column) for the terrain model with magnetisation of declination 188°, inclination +57°. Solid lines – forward computed from the terrain model, dotted line – with added noise, dashed line – output from the inversion of the input terrain model data with added noise.

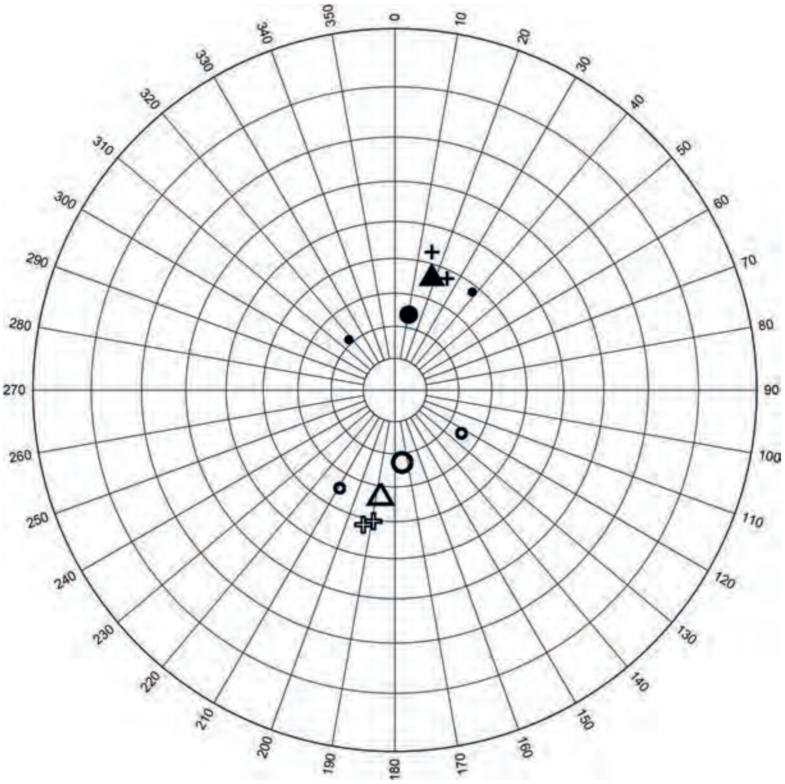

Fig. 11.18. Magnetisation directions: Input magnetisations (triangles), flightline inversions (small circles), average of the two flightline inversions (larger circles) and ground track inversions (crosses). Open symbols are positive inclination, closed symbols are negative inclination.

Table 11.1. Magnetisation direction estimates from inversion of the ground data around the feature and the aerial data above it.

Survey	Magnetisation	Intensity A/m	Declination°	Inclination°	Error°
Ground					
west track	A	4.7	25	−52	5
	B	3.2	193	48	9
east track	A	4.2	15	−47	7
	B	3.8	189	50	7
Aerial					
line AB	A	2.7	318	−69	31
	B	2.5	123	65	31
line CD	A	3.6	38	−52	12
	B	3.3	209	55	12
mean	A		11	−66	4
	B		174	67	12

Figure 11.17 shows model-computed magnetic components with and without noise and the simplified model-computed components derived from inversion of the noise added data. The amplitude of the magnetic field variations at this elevation over the terrain are an order of magnitude higher than on the ground tracks around it, with an average range of 526 nT and average standard deviation of 127 nT. To accommodate the greater challenges of making vector measurements from a moving platform we added a higher noise level of 30 nT standard deviation to the input field data. The magnetisation estimates recovered from inversion of the data on each profile are listed in Table 11.1. In this case there are systematic differences between results for both input magnetisations on each line, with errors of 31° on line AB and 12° on line CD. These errors are not due to the added random noise but to the horizontal top of the simplified inversion model that misrepresents the part of the terrain closest to the overflight measurements. This misrepresentation is more significant on profile AB than on profile CD. In practice it will be the validity of the terrain model in representing the spatial distribution of magnetisation that limits reliability in recovering the magnetisation direction.

11.5 CONCLUSIONS

Over the Miocene age Lamington volcanics in north-east New South Wales there is positive and negative correlation between terrain elevation and TMI, due to magnetisation that is respectively parallel and anti-parallel to the geomagnetic field. We have recovered estimates of these magnetisations from inversion of the magnetic field data using spatial models of magnetisation derived from the digital elevation model (DEM). Recovery of magnetisation direction is more challenging where magnetisation is buried and inversion has to determine its distribution as well as its intensity and direction. We show that the advantage of a known spatial model of magnetisation is sufficient to allow recovery of reasonable estimates of magnetisation direction from inversion of a single profile of TMI (or any other single component) and more tightly constrained estimation of magnetisation direction from inversion of single profiles of multi-component data. Use of vector component data is impractical in the strong background field of the Earth that penalises even slight misorientation of the sensor but is feasible in the weak background fields of Mars where the magnetic field variations are predominantly the signal of interest. We use a local Martian terrain feature of width 20–25 km and height 800 m to generate synthetic three-component magnetic field data and show that input magnetisation directions can be reasonably recovered from analysis of sparse measurements along either rover tracks around that feature or overflights above it. The practicality of these methods depends primarily on the strength of magnetisation and its geological distribution in relationship to terrain features.

REFERENCES

Albee AL, Arvidson RE, Palluconi F, Thorpe T (2001) Overview of the Mars Global Surveyor mission. *Journal of Geophysical Research* 106(E10), 23291–23316. doi:10.1029/2000JE001306

Blakely RJ 1995, Potential Theory in Gravity and Magnetic Applications: Cambridge University Press.

Brown RE, Cranfield LC, Denaro TJ, Burrows PE, Henley HF, Stroud WJ, Brownlow JW (2007) Warwick - Tweed Heads 1:250 000 Metallogenic Map SH/56 2–3. Geological Survey of New South Wales, Maitland and Geological Survey of Queensland, Brisbane.

Duggan MD, Mason DR (1978) Stratigraphy of the Lamington Volcanics in far Northeastern New South Wales. *Journal of the Geological Society of Australia* 25, 65–73. doi:10.1080/00167617808729014

Mittelholz A, Johnson CL, Feinberg JM, Langlais B, Phillips RJ (2020) Timing of the martian dynamo: New constraints for a core field 4.5 and 3.7 Ga ago. *Science Advances* 6, 1–7.

Neumann GA, Rowlands DD, Lemoine FG, Smith DE, Zuber MT (2001) Crossover analysis of Mars Orbiter Laser Altimeter data. *Journal of Geophysical Research* 106(E10), 23753–23768. doi:10.1029/2000JE001381

Neumann GA, Smith DE, Zuber MT (2003) Two Mars years of clouds detected by the Mars Orbiter Laser Altimeter. *Journal of Geophysical Research* 108(E4), 5023. doi:10.1029/2002JE001849

Schubert G, Russell CT, Moore WB (2000) Timing of the Martian dynamo. *Nature* 408, 666–667. doi:10.1038/35047163

Smith DE, Zuber MT, Frey HV, Garvin JB, Head JW, Muhleman DO, Pettengill GH, *et al*. (2001) Mars Orbiter Laser Altimeter – experiment summary after the first year of global mapping of Mars. *Journal of Geophysical Research* 106(E10), 23689–23722. doi:10.1029/2000JE001364